International Journal of Computer Assisted Radiology and Surgery (2018) 13:1781–1793
https://doi.org/10.1007/s11548-018-1848-x

ORIGINAL ARTICLE

Semiautomatic neck curve reconstruction for intracranial aneurysm rupture risk assessment based on morphological parameters

Sylvia Saalfeld[1,4] · Philipp Berg[2,4] · Annika Niemann[1] · Maria Luz[1] · Bernhard Preim[1,4] · Oliver Beuing[3,4]

Received: 10 January 2018 / Accepted: 14 August 2018 / Published online: 29 August 2018

Abstract

Purpose Morphological parameters of intracranial aneurysms (IAs) are well established for rupture risk assessment. However, a manual measurement is error-prone, not reproducible and cumbersome. For an automatic extraction of morphological parameters, a 3D neck curve reconstruction approach to delineate the aneurysm from the parent vessel is required.

Methods We present a 3D semiautomatic aneurysm neck curve reconstruction for the automatic extraction of morphological parameters which was developed and evaluated with an experienced neuroradiologist. We calculate common parameters from the literature and include two novel angle-based parameters: the *characteristic dome point angle* and the *angle difference of base points*.

Results We applied our method to 100 IAs acquired with rotational angiography in clinical routine. For validation, we compared our approach to manual segmentations yielding highly significant correlations. We analyzed 95 of these datasets regarding rupture state. Statistically significant differences were found in ruptured and unruptured groups for maximum diameter, maximum height, aspect ratio and the characteristic dome point angle. These parameters were also found to statistically significantly correlate with each other.

Conclusions The new 3D neck curve reconstruction provides robust results for all datasets. The reproducibility depends on the vessel tree centerline and the user input for the initial dome point and parameters characterizing the aneurysm neck region. The characteristic dome point angle as a new metric regarding rupture risk assessment can be extracted. It requires less computational effort than the complete neck curve reconstruction.

Keywords Intracranial aneurysm · Neck curve · Morphological parameters · Rupture risk assessment

Introduction

Rupture risk assessment for intracranial aneurysms (IAs) remains challenging, since vascular malformations are highly individual with respect to their shape and underlie varying hemodynamic conditions [1]. 2D measurements (e.g., ostium size, dome-to-neck ratio and aspect ratio) are carried out and are used as rupture risk indicators in clinical routine [2, 3]. However, these measurements are highly user—as well as image-dependent, and the viewing angle for the 2D projections influences the resulting parameter values [4].

To overcome this problem, several studies considering 3D shape parameters of IAs were carried out during the last years [5–10]. Raghavan et al. [9] compared five size and eight shape indices with respect to the rupture status. They showed that none of the size parameters were significantly different between the ruptured and unruptured group, while five shape indices reached significance. A total of 119 aneurysm models were analyzed by Xiang et al. [11]. They identified the size ratio as the only independently significant factor in their morphology model. However, shape complexity parameters such as undulation index, ellipticity index and non-sphericity index were also significantly different between ruptured and unruptured aneurysms. Lv et al. [7] focused on morphological discriminants for the rupture

✉ Sylvia Saalfeld
sylvia.saalfeld@ovgu.de

1 Department of Simulation and Graphics, Otto-von-Guericke University of Magdeburg, Magdeburg, Germany

2 Department of Fluid Dynamics and Technical Flows, Otto-von-Guericke University of Magdeburg, Magdeburg, Germany

3 Department of Neuroradiology, University Hospital of Magdeburg, Magdeburg, Germany

4 Research Campus STIMULATE, Magdeburg, Germany

status of posterior communicating artery aneurysms. They evaluated 129 cases, and their univariate analysis revealed that the size of aneurysm dome, the aspect ratio, the size ratio as well as the dome-to-neck ratio were significantly associated with rupture. Recently, Varble et al. [10] used a database of 311 aneurysms to quantify morphological characteristics of patient-specific IAs. They could demonstrate that only the size ratio was different between internal carotid artery (ICA) aneurysms, middle cerebral artery aneurysms and anterior/posterior communication artery aneurysms. Furthermore, they concluded that ICA aneurysms are subject to less rupture-prone morphological characteristics in comparison with other locations within the Circle of Willis.

Overall, it can be noticed that several drawbacks occur. First, some studies considered only a low number of aneurysms (e.g., 27 IAs in [9] and 45 IAs in [5]). Additionally, the separation of the aneurysm from the healthy parent vessel is often realized using a (planar) cut-plane [6, 9, 11] instead of an anatomical neck curve (NC) that also accounts for the highly variational aneurysm shapes including possible bulges. Furthermore, the influence of imaging parameters like reconstruction kernels also influences the morphology [12].

As a consequence, relevant parameters such as diameters, surfaces, volumes as well as derived ratios can be clearly over- or underestimated compared to the actual situation leading to wrong conclusions with respect to the rupture risk assessment.

The recent study addresses those issues and provides an analysis, which is based on high-quality data. Specifically, 3D segmentations of 100 IAs were carried out based on extensive technical experience [13–16]. We present a semiautomatic NC reconstruction that allows for automatic extraction of the morphological parameters. An evaluation is carried out based on 100 manually drawn NCs. Finally, a statistical analysis identifies relevant shape parameters to differentiate between ruptured and unruptured aneurysms.

Materials and methods

In this section, we describe the acquired datasets and the semiautomatic NC reconstruction. Afterward, the extraction of morphological parameters is described.

Data acquisition and segmentation

The datasets included in this study comprise 100 IA datasets from 70 patients (age: 33–93 years, 14 male and 56 female). The maximum height of the aneurysms ranged from 1.63 to 11.72 mm, with a mean value of 5.12 mm and a median value of 4.69 mm. The maximum diameter of the aneurysms ranged from 2.29 to 15.60 mm with a mean value of 6.58 mm and a median value of 5.86 mm. Fifty-three of these aneurysms were ruptured, whereas 42 aneurysms were not ruptured. The status of the remaining five aneurysms was unclear since they were acquired during clinical routine. All patients included in this study underwent digital subtraction angiography (DSA) at the University Hospital Magdeburg, Germany, because of ruptured or incidentally discovered aneurysms. The examinations were part of the necessary clinical work-up and were performed on an Artis Q (Siemens Healthineers, Forchheim, Germany). The imaging protocol included a 3D rotational angiography (3D RA) in each patient, which is considered the gold standard in diagnostics and post-processing due to its high resolution. The 3D vascular trees were reconstructed from the data of the 3D RA using a threshold-based segmentation as proposed in [17], and then converted into a 3D triangulated surface mesh. Based on the surface mesh, the vessel's centerline was semi-automatically extracted with the vascular modeling toolkit (VMTK, vmtk.org) [18]. Hence, the user manually selects the seed points by selecting the inlet and all outlets. The use of the data and its analysis comply with the guidelines of the local ethics committee.

For the evaluation of our approach, a manual NC segmentation for each of the 100 IAs was acquired by an experienced neuroradiologist. Each IA surface model was loaded into Blender 2.74 (Blender Foundation, https://www.blender.org/), and the NC was manually placed using the "knife" tool. The user can arbitrarily place lines onto the surface mesh which were manually corrected to obtain a closed NC. The obtained NCs were interpreted as gold standard for the evaluation of our approach.

Semiautomatic neck curve reconstruction

Our framework is implemented in MATLAB (MathWorks, Natick, USA). Thus, the implementation is speed up by using vectorized data structures as well as MATLAB's Parallel Computing Toolbox, which supports image processing operations on the GPU.

For the automatic NC extraction, we discussed basic requirements for the resulting curves based on manually drawn NC from clinical experts. Inspired by the approach of Neugebauer et al. [19] and our discussions, we aim at an ostium plane that is roughly bent around the centerline of the parent vessel. Hence, we decide to employ the two nearest vessel branches to the aneurysm itself. Compliant to this approach, we also extract two points on the parent vessel surface that are located before (P_1) and after (P_2) the bulging of the aneurysm (between centerline and dome), since these points were always crossed by the manual NCs.

To describe the bending of the NC, we require two additional points P_3 and P_4. The bending of the NC depends on the vessel radius and the aneurysm shape. The connected points yield the NC. Since the neck is the smallest part at

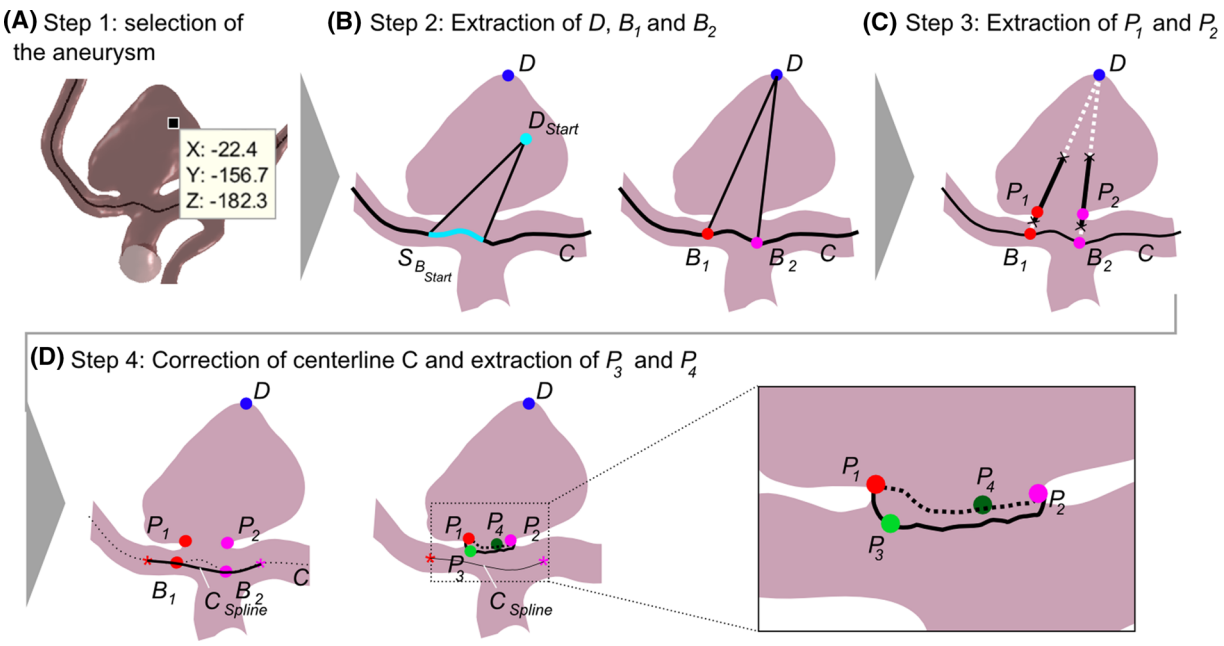

Fig. 1 Pipeline for the semiautomatic NC reconstruction. First, the user clicks in the scene on the aneurysm to define D_{Start} (**a**). D_{Start} is used to extract $S_{B_{\text{Start}}}$ on the centerline C and the dome D. Next, the base points B_1 and B_2 are extracted (**b**). Afterward, P_1 and P_2 are determined (**c**). C is replaced with a spline-based corrected centerline C_{Spline}. P_3 and P_4 are reconstructed (**d**), which are connected to the NC (see inlay)

the transition from parent vessel to aneurysm, the connection of these points is restricted to shortest paths on the aneurysm surface. Although the work by Neugebauer et al. [19] used these four characteristic points as well, we use different extraction methods as well as a modified connection approach for them.

The workflow is illustrated in Fig. 1 and comprises four steps:

- *Step 1* One-click selection of the aneurysm (see Fig. 1a).
- *Step 2* Extraction of the dome point D and base points B_1 and B_2 (see Fig. 1b).
- *Step 3* Extraction of P_1 and P_2 at the aneurysm surface (see Fig. 1c).
- *Step 4* Extraction of P_3 and P_4 to reconstruct the NC (see Fig. 1d).

Step 1: One-click selection of the aneurysm

In Step 1, the user selects the aneurysm with a single click which also initializes our method. We refer with D_{Start} to the selected position (recall Fig. 1a). D_{Start} should be near the actual dome point D. The dome point D refers to the aneurysm point with largest distance to the parent vessel. To speed up the subsequent steps, only parts of the surface mesh and centerline within 15 mm distance to D_{Start} are used. The user can increase or decrease this value.

Step 2: Extraction of the dome point *D* and the base points B_1 and B_2

In Step 2, the base points B_1 and B_2 and the dome point D are extracted (see Fig. 1b). First, the set of points $S_{B_{\text{Start}}}$ is determined, where $S_{B_{\text{Start}}}$ comprises all points B_i of the centerline such that the vector $\overrightarrow{B_i D_{\text{Start}}}$ does not intersect the triangle mesh (recall Fig. 1b). We set D to D_{Start}. If any neighbored vertex N_i of D exhibits a larger average distance to $S_{B_{\text{Start}}}$, we set $D = N_i$ and iteratively repeat this process until D is the most distant point to $S_{B_{\text{Start}}}$. Two vertices are neighbored if they share an edge on the triangle mesh. We extract S_B comprising all points B_i of the centerline, where $\overrightarrow{B_i D}$ does not intersect the triangle mesh.

Next, B_1 and B_2 are extracted from S_B, see Fig. 2. To account for bifurcation aneurysms including branching centerlines, three points T_1, T_2 and T_3 are extracted. T_1 and T_2 form the pair of points from S_B with the maximum possible distance to each other. T_3 is the point with maximum distance to T_1 and T_2. If T_1, T_2 and T_3 form a non-degenerated triangle, B_1 and B_2 are selected as the two points from T_1 to T_3 with shortest distance to D (recall Fig. 2). Otherwise, B_1 and B_2 are set to the points with largest distance to each other. We empirically define T_1, T_2 and T_3 to form a degenerated triangle if the longest triangle edge e_1 and the remaining edges e_2 and e_3 fulfill $0.8 \times e_1 < e_2 + e_3 < 1.2 \times e_1$.

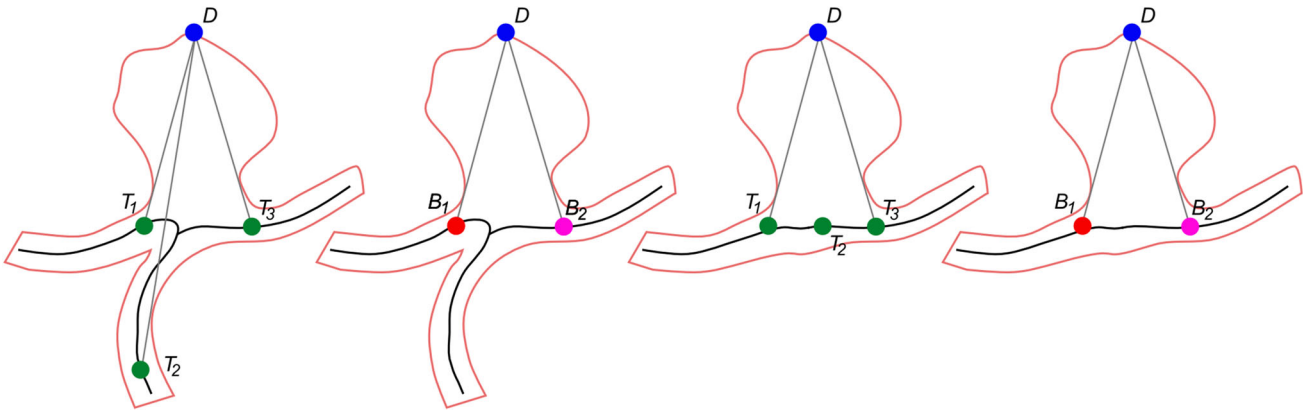

Fig. 2 Extraction of B_1 and B_2 from T_1, T_2 and T_3 for two aneurysms. For bifurcation aneurysms, T_1, T_2 and T_3 form a triangle and B_1 and B_2 exhibit smallest distances to D (left). For sidewall aneurysms, T_1, T_2 and T_3 form a thin and degenerated triangle (right)

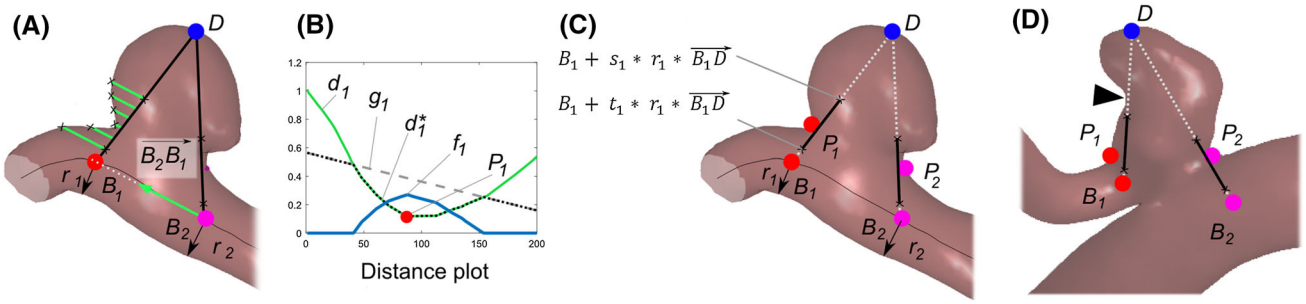

Fig. 3 Extraction of P_1 and P_2. The distances to the surface mesh starting at segment $\overline{B_1D}$ in direction $\overrightarrow{B_2B_1}$ are extracted as intersection points (**a**). They are plotted in the distance plots as d_1 from which g_1, $d_1{}^*$ and f_1 are extracted (**b**). The maximum of f_1 defines the position of P_1. P_2 is extracted accordingly. As a result, P_1 and P_2 are depicted with the original mesh (**c**). Example case where a false position (see arrowhead) has the shortest distance to $\overline{B_1D}$ (**d**). With the restriction to the aneurysm neck region based on t_1, s_1 and r_1, P_1 is correctly determined

Extraction of P_1 and P_2 at the aneurysm surface

In Step 3, points P_1 and P_2 are extracted (see Fig. 1c). P_1 and P_2 are located at the aneurysm neck along the parent vessel. They are characterized by minimum distances to the segments $\overline{B_1D}$ and $\overline{B_2D}$ near the aneurysm neck region.

For the calculation of P_1, we cast rays in direction $\overrightarrow{B_2B_1}$ by sampling the segment $\overline{B_1D}$ and determine the distances d_1 to the intersections with the surface, see Fig. 3. Possible neck points are characterized by a local minimum of d_1 near the aneurysm neck region. To determine this region, only points originating between $t_1 \times r_1$ and $s_1 \times r_1$ on the segment $\overline{B_1D}$ are considered, where r_1 is the vessel radius at B_1. For the vessel radii extraction, rays are cast perpendicular to the centerline at B_1 and the median distance to the surface is assigned to r_1. We empirically set $t_1 = 0.5$ and $s_1 = 2.0$. These parameters can be adapted by the user since it may occur that the vessel radii cannot be correctly determined due to the large variations considering the aneurysm shapes.

As a result, d_1 is restricted to the aneurysm neck region. We plot d_1 in a distance plot (see Fig. 3b). We fit a line through d_1 yielding g_1. Since we are only interested in minima, we set all values $d_1(x) < g_1(x)$ to $g_1(x)$ and obtain $d_1{}^*$. The position of P_1 is defined at the maximum position of $f_1(x)$, where $f_1(x)$ provides the shortest distance for each point $(x; d_1{}^*)$ to the line defined by g_1. Once we obtained x, we extract the corresponding intersection point with the surface mesh and obtain P_1 (see Fig. 3c).

This method works well for large variations of aneurysm shapes. For example, the specific aneurysm shape yields various minimum distances to $\overline{B_1D}$ in Fig. 3d. In particular, a location near the dome would result in a false candidate for P_1 (see arrowhead, Fig. 3d). Due to the restriction to the aneurysm neck region (based on parameters t_1 and s_1), this candidate is not considered for P_1.

Analogously, we repeat this procedure for B_2 to obtain d_2 and finally P_2.

Extraction of P_3 and P_4 of the neck curve

In Step 4, we extract P_3 and P_4 as the last two sample points for the NC. The centerline is distorted caused by the aneurysm sac. To compensate for this distortion, we gather points of the centerline of B_1 and B_2 from the outside, i.e.,

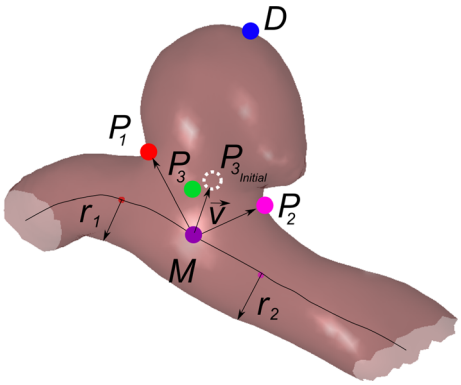

Fig. 4 Illustration of the extraction of P_3: $P_{3_{\text{initial}}}$ is determined inside the aneurysm (see dashed circle), and P_3 is identified as nearest surface point to $P_{3_{\text{initial}}}$

which are not in between them. We employ these sample points to fit a cubic spline curve and replace centerline points between B_1 and B_2 with the corresponding spline points (see Fig. 1d). Thus, we interpolate the points in between assuming continuity in the curve and its gradient direction.

Next, the initial position of P_3 is extracted. Therefore, we determine the point M which is equidistant to B_1 and B_2 and lies on the centerline, see Fig. 4. The initial position of P_3 is denoted as $P_{3_{\text{initial}}}$ and interpolated by $P_{3_{\text{initial}}} = M + \frac{1}{2}(r_1 + r_2) * \vec{v}$, where $\vec{v}$ is the normalized vector of $\overrightarrow{MP_1} + \overrightarrow{MP_2}$. Then, P_3 is identified as nearest surface point to $P_{3_{\text{initial}}}$.

To obtain the shortest NC, we iteratively move P_3 along the surface mesh, in case one of its neighbors yields a shorter NC than the initial position. That means, we extract for each neighbor N_i of P_3 the shortest paths from P_1 to N_i and from N_i to P_2. If we obtain a shorter path, we set $P_3 = N_i$ and repeat the procedure. For finding the shortest connections, we interpret the surface mesh as graph structure and use MATLAB's *shortestpath*() function based on [20].

P_4 is extracted by rotating the vector $\overrightarrow{MP_3}$ around the axis $\overrightarrow{B_2B_1}$ with an angle in between 180° and 270°. We empirically set this angle to 220°. In accordance to P_3, P_4 is moved as long as a neighbor exists that yields a shorter path from P_1 to P_2 containing this point. However, the large variations of aneurysm anatomies lead to cases where the NC is defined under the parent vessel, see Fig. 5. To overcome this problem, we automatically extract exclusion points. We determine P_1' and P_2' opposite P_1 and P_2. $P_1' = C_{P_1} - \overrightarrow{C_{P_1}P_1}$ and $P_2' = C_{P_2} - \overrightarrow{C_{P_2}P_2}$, where C_{P_1} and C_{P_2} are nearest points on the centerline to P_1 and P_2. We then exclude all surface mesh points within 1 mm distance to P_1' and P_2' for the shortest path search. We furthermore extract the closest pair of points Q_1 and Q_2 (where Q_1 is within 1 mm distance to P_1' and Q_2 is within distance to P_2'), extract the shortest path between these points and add the path vertices to the exclusion points. Thus, the NC cannot intersect with these paths. The final NC is provided by the shortest paths from P_1 to P_3, P_3 to P_2, P_2 to P_4 and P_4 to P_1 (recall Fig. 1d).

Although our approach works for a wide variety of saccular and bifurcation IAs, it requires a pronounced neck curve. Very small aneurysms may not exhibit a visible distinguish-

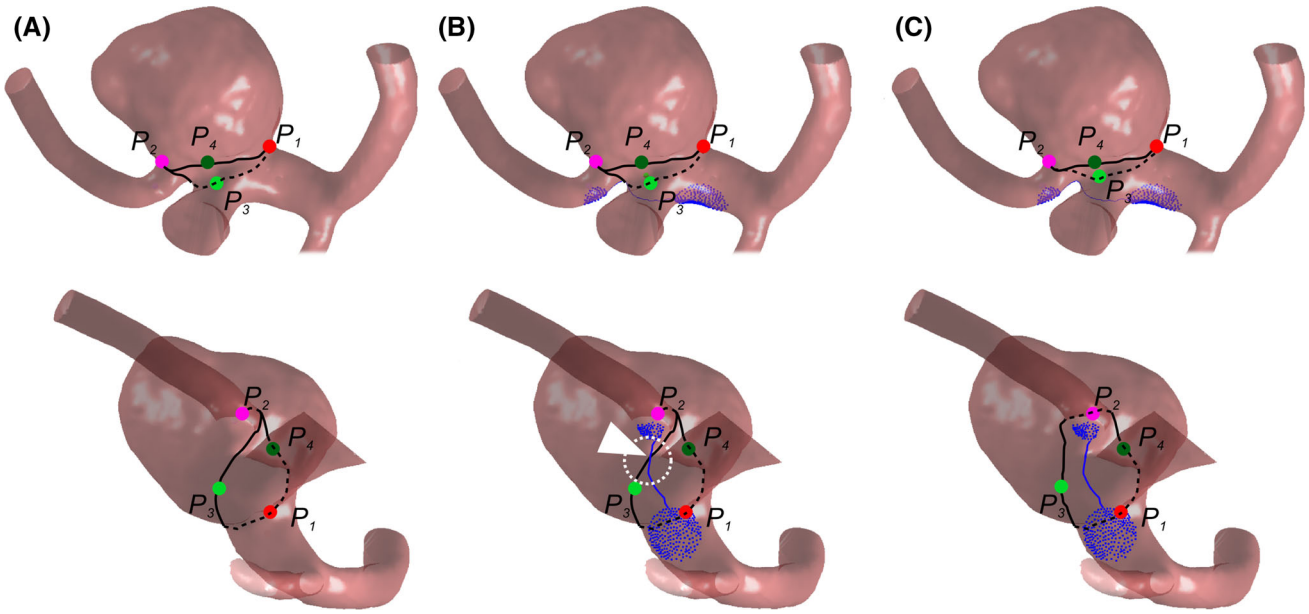

Fig. 5 Example of an aneurysm at the posterior communicating artery from the front (top row) and the bottom (bottom row). The neck curve without exclusion points would be found under the parent vessel (**a**). The excluded vertices and the excluded path are illustrated in blue (**b**). The excluded path intersects with the shortest path from P_3 to P_2 (see arrowhead). After exclusion, the correct neck curve is extracted (**c**)

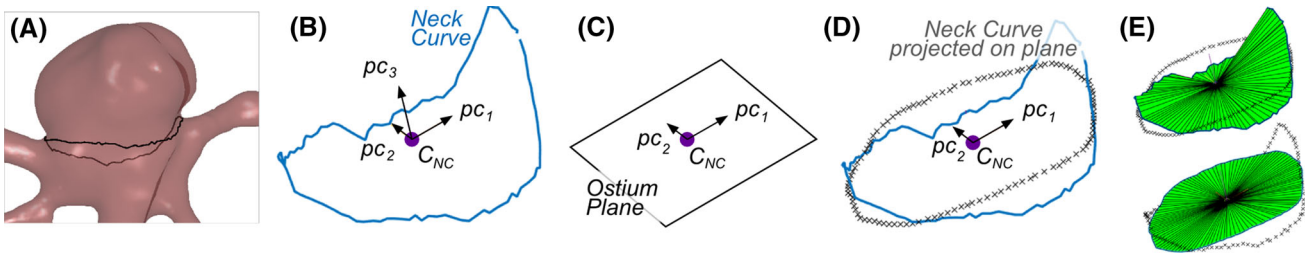

Fig. 6 Extraction of the ostium plane for a basilar artery aneurysm (**a**). From the NC points, the mean C_{NC} and the principal components pc_1, pc_2 and pc_3 are extracted (**b**). The ostium plane is defined by C_{NC}, pc_1 and pc_2 (**c**). The NC can be projected on this plane (**d**). Triangulation of the NC and the projected NC yields two surfaces (**e**)

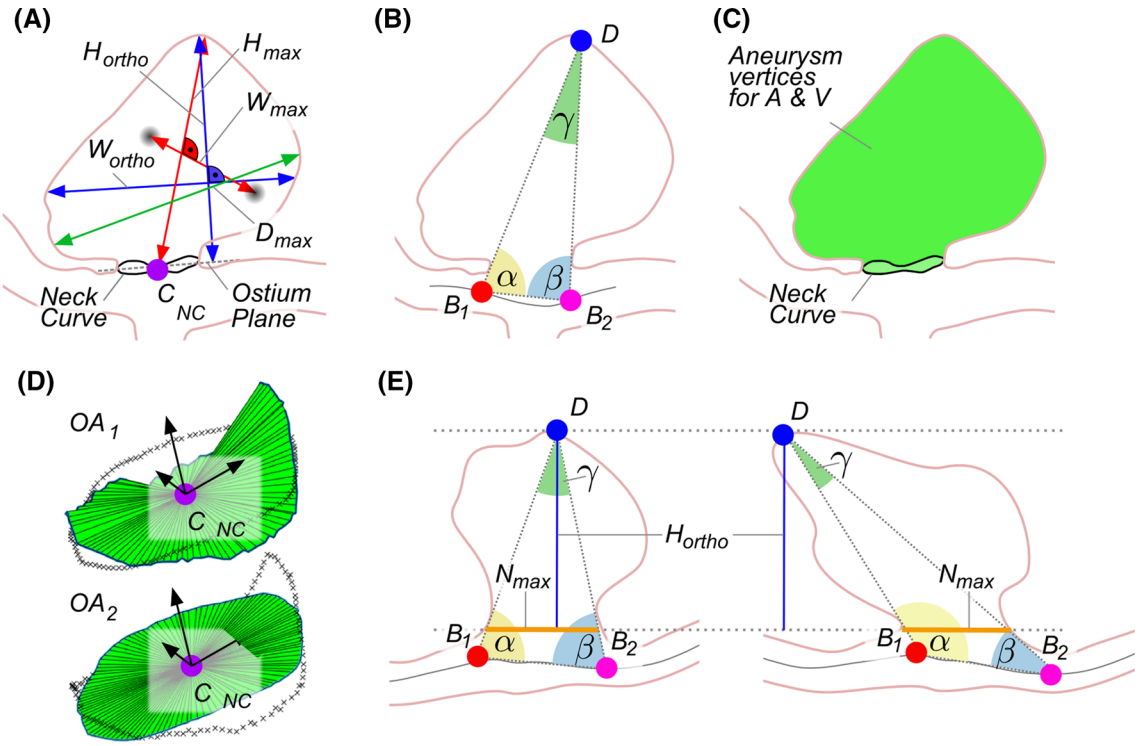

Fig. 7 Illustration of the morphological parameters H_{max}, W_{max}, H_{ortho}, W_{ortho} and D_{max} (**a**), as well as the angles α, β and γ between the base points B_1 and B_2 and the dome D (**b**). The NC separates the aneurysm vertices from the parent mesh to approximate A and V (**c**). The surface area of the ostium is extracted for the reconstructed NC (OA_1) as well as for the projected NC (OA_2) (**d**). The angle-related parameters account for the tilting of the aneurysm (**e**). Here, the aspect ratio is identical, but γ and $\Delta_{\alpha\beta}$ differ

able neck yet. For these cases, the user can manually place P_3 and P_4 on the surface and the final NC is again provided by the shortest paths from P_1 to P_3, P_3 to P_2, P_2 to P_4 and P_4 to P_1. For all cases of the presented study, P_3 and P_4 were automatically determined.

Morphological analysis

With the extracted NC, we can automatically and robustly determine common morphological parameters [5, 9]. Since many parameters from the literature require a planar ostium plane, we provide this plane as well. We denote the center of the neck curve, i.e., the mean of all neck curve points using C_{NC}. Next, we employ a principal component analysis (PCA) to all neck curve points yielding principal component vectors $\overrightarrow{pc_1}$, $\overrightarrow{pc_2}$, and $\overrightarrow{pc_3}$, see Fig. 6. First, we define the ostium plane as plane through C_{NC} with the plane vectors $\overrightarrow{pc_1}$ and $\overrightarrow{pc_2}$. Second, we project each NC point onto this plane by determining the intersection point in direction of $\overrightarrow{pc_3}$, which equals the plane's normal (recall Fig. 6).

We extract the following 20 parameters, which are illustrated in Fig. 7.

- A the area of the aneurysm (without the ostium), i.e., the surface area of all triangles separated by the neck curve.
- V the volume of the aneurysm (the NC is triangulated by connecting all neck curve points with C_{NC}).
- OA_1 area of the ostium (the NC is triangulated by connecting all neck curve points with C_{NC}).
- OA_2 area of the ostium with the NC projected onto a plane.
- $D_{\max}$ maximum diameter of the aneurysm, i.e., the distance of the two most distant points of the aneurysm.
- $H_{\max}$ maximum height, i.e., maximum distance of an aneurysm point to C_{NC}.
- $W_{\max}$ maximum width of the aneurysm perpendicular to $H_{\max}$. This distance is obtained by connecting C_{NC} with the point corresponding to $H_{\max}$ and sampling rays perpendicular to this connection.
- H_{ortho} height of the aneurysm approximated as length of the ray perpendicular to the ostium plane starting from C_{NC}.
- W_{ortho} maximum width parallel to the projected ostium plane.
- $N_{\max}$ maximum NC diameter, i.e., the maximum possible distance of two NC points.
- N_{avg} average NC diameter, i.e., the mean distance of C_{NC} to the NC points.
- AR_1 the aspect ratio: $H_{\mathrm{ortho}}/N_{\max}$.
- AR_2 the aspect ratio: $H_{\mathrm{ortho}}/N_{\mathrm{avg}}$.
- V_{CH} volume of the convex hull of the aneurysm vertices.
- A_{CH} area of the convex hull of the aneurysm vertices.
- EI the ellipticity index: $\mathrm{EI} = 1 - (18\pi)^{1/3} V_{\mathrm{CH}}^{2/3}/A_{\mathrm{CH}}$.
- NSI the non-sphericity index: $\mathrm{NSI} = 1 - (18\pi)^{1/3} V^{2/3}/A$.
- UI the undulation index: $\mathrm{UI} = 1 - \left(\frac{V}{\mathrm{CH}_V}\right)$.
- $\Delta_{\alpha\beta}$ absolute value of difference between the angles α (i.e., the angle between $\overrightarrow{B_1 D}$ and $\overrightarrow{B_1 B_2}$) and β (i.e., the angle between $\overrightarrow{B_1 B_2}$ and $\overrightarrow{D B_2}$).
- γ angle at D, i.e., between $\overrightarrow{D B_1}$ and $\overrightarrow{D B_2}$.

It must be noted that all of these parameters can be automatically extracted based on a given NC and no manual user interaction is necessary. Furthermore, parameters except $\Delta_{\alpha\beta}$ and γ were already introduced in the literature. During the NC detection development, the parameters $\Delta_{\alpha\beta}$ and γ were identified as well suited to characterize tilted aneurysms with respect to their parent arteries. In contrast to AR_1 and AR_2, γ describes the height and width ratio of aneurysms and their tilting at the same time (recall Fig. 7e). Furthermore, $\Delta_{\alpha\beta}$ provides information about the tilting itself. We carried out statistical evaluation to assess whether ruptured and unruptured aneurysms differ w.r.t. their morphological parameters. All tests were carried out with SPSS 22.0 (IBM, New York, USA).

Evaluation

Our semiautomatic NC reconstruction was applied to all 100 datasets, and we could automatically extract the morphological parameters for each aneurysm. First, the comparison of the semiautomatic NC to the manually drawn curves is carried out. Afterward, the results of the morphologic parameter extraction w.r.t. rupture state are presented.

Comparison of semiautomatic and manual NC approach

We compared the semi-automatically determined NC ($\mathrm{NC}_{\mathrm{new}}$) to the manually segmented one ($\mathrm{NC}_{\mathrm{manual}}$) for each aneurysm. Therefore, we employ the average distance and standard deviation between two *NC*s presented by Cárdenes et al. [21]. The resulting average distances are provided in the box plot (Fig. 8), with a median value of 1.35 mm. In Fig. 9, the average distances w.r.t. the maximum aneurysm diameter are depicted separately. We use the result of this metric to identify the three cases with lowest and highest average differences, recall Fig. 8. Comparison of the average distances of the manual and semiautomatic NC to the individual aneurysm's maximum diameter yields the following results: 25% of the cases exhibit errors smaller than 14%, 50% smaller than 25% and 75% smaller than 36% of the maximum diameter.

The clinician requested similar results concerning the morphological parameters based on $\mathrm{NC}_{\mathrm{manual}}$ and $\mathrm{NC}_{\mathrm{new}}$. We conducted a correlation analysis based on the Pearson correlation coefficient (PCC) for the parameters A, V, OA_1, OA_2, $D_{\max}$, $H_{\max}$, $W_{\max}$, H_{ortho}, W_{ortho}, $N_{\max}$ and N_{avg} since these are most often used in clinical practice.

Our analysis yields significant correlations with $p < 0.001$ for all parameters: $\mathrm{PCC}(A) = 0.974$ (i.e., the $\mathrm{PCC}(A)$ denotes the PCC for parameter A based on $\mathrm{NC}_{\mathrm{manual}}$ and A based on $\mathrm{NC}_{\mathrm{new}}$), $\mathrm{PCC}(V) = 0.940$, $\mathrm{PCC}(\mathrm{OA}_1) = 0.971$, $\mathrm{PCC}(\mathrm{OA}_2) = 0.961$ ($p = 0.000$), $\mathrm{PCC}(D_{\max}) = 0.934$, $\mathrm{PCC}(H_{\max}) = 0.960$, $\mathrm{PCC}(W_{\max}) = 0.962$, $\mathrm{PCC}(H_{\mathrm{ortho}}) = 0.951$, $\mathrm{PCC}(W_{\mathrm{ortho}}) = 0.947$, $\mathrm{PCC}(N_{\max}) = 0.938$ and $\mathrm{PCC}(N_{\mathrm{avg}}) = 0.963$. As a result, we can conclude that $\mathrm{NC}_{\mathrm{manual}}$ and $\mathrm{NC}_{\mathrm{new}}$ yield significantly correlating parameter values for the morphologic parameters and the usage of our semiautomatic NC approach is justified.

Results of morphological parameter analysis

For the statistical evaluation, we only used 95 aneurysms with clear rupture state. Unclear rupture states arise if a patient suffered from multiple aneurysms and the ruptured one could not be clearly identified. First, an analysis for normal distribution was carried out; the Kolmogorov–Smirnov test did

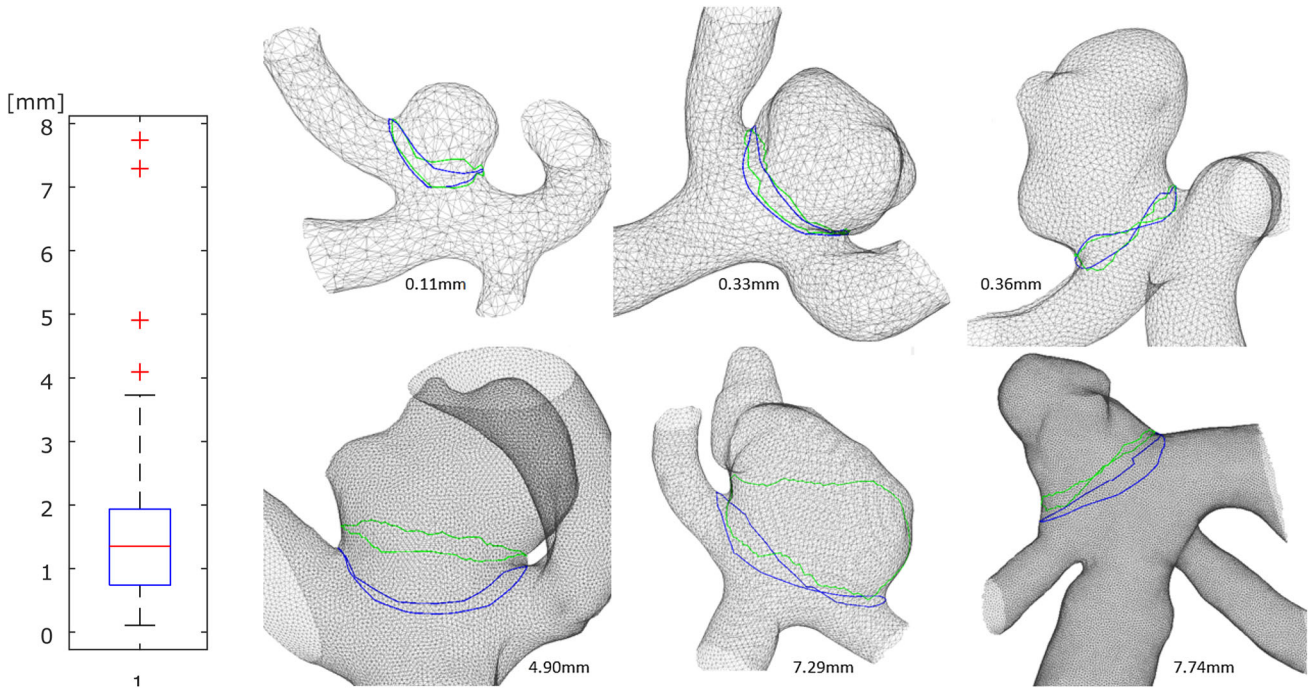

Fig. 8 Boxplot of the extracted averaged distances (in mm) between manual and semiautomatic NCs for the 100 tested datasets (median = 1.53 mm, 25th percentile = 0.74 mm, 75th percentile = 1.94 mm, left). Depiction of the semiautomatic NC results for the three best (right, top row) and three worst (right, bottom row) datasets with respect to average differences between semiautomatic NC (green) and manual NC (blue). The average differences are provided for each of the cases in the figure

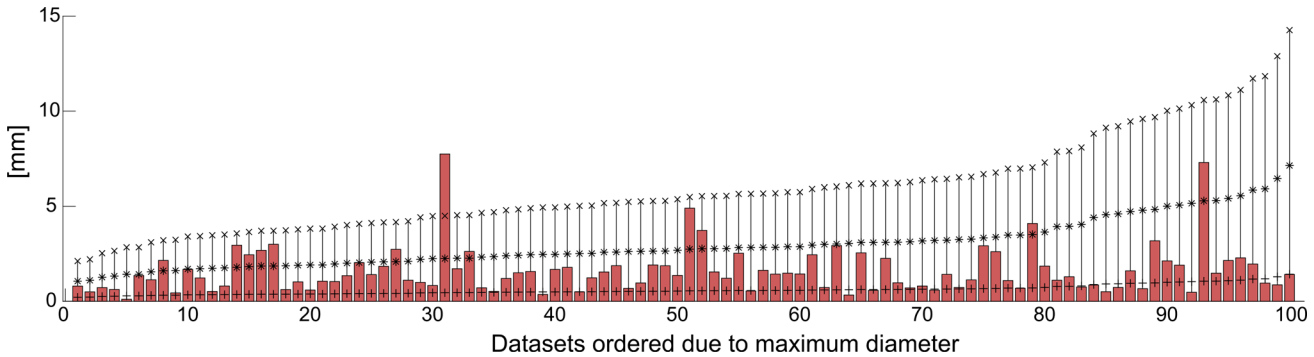

Fig. 9 Bar plot of the average distance between manual and semiautomatic NC for all 100 datasets in relation to the maximum aneurysm diameter: the markers +, * and *x* refer to 10%, 50% and 100% of the maximum aneurysm diameter, respectively

not show normal distributed data for each of the provided parameters.

Therefore, the nonparametric Mann–Whitney-*U* test was applied for each parameter, see Table 1. The ruptured and unruptured aneurysms significantly differ regarding the parameters D_{max}, H_{max}, AR_1, AR_2 and γ. Mean value and standard deviation are provided in Table 2, and box plots are depicted in Fig. 10. The box plots for the unruptured and ruptured IAs present the parameter distribution based on NC_{manual} and NC_{new}. Subsequently, we calculated the correlation between these parameters based on the Pearson correlation coefficient (PCC). Interestingly, all of these five parameters significantly correlate with each other: $PCC(D_{max}; H_{max}) = 0.972$, $PCC(D_{max}; AR_1) = 0.473$, $PCC(D_{max}; AR_2) = 0.498$, $PCC(D_{max}; \gamma) = -0.343$, $PCC(H_{max}; AR_1) = 0.646$, $PCC(H_{max}; AR_2) = 0.662$, $PCC(H_{max}; \gamma) = -0.500$, $PCC(AR_1; AR_2) = 0.980$, $PCC(AR_1; \gamma) = -0.822$, and $PCC(AR_2; \gamma) = -0.812$, with $p < 0.01$ for all tests.

Discussion

This study introduces a new approach to semi-automatically reconstruct the neck curve of patient-specific IAs. It was adapted to 100 IAs with varying sizes, locations and type

Table 1 Result of the nonparametric Mann–Whitney-*U* (MWU) test for the morphological parameters

Parameter	MWU	*Z*	*p*
A	867	−1.803	0.071
V	903	−1.533	0.125
OA_1	990	−0.879	0.379
OA_2	992	−0.864	0.388
D_{max}	845	−1.969	0.049*
H_{max}	795	−2.344	0.019*
W_{max}	916	−1.435	0.151
H_{ortho}	854	−1.901	0.057
W_{ortho}	934	−1.300	0.194
N_{max}	1031	−0.571	0.568
N_{avg}	985	−0.917	0.359
AR_1	785	−2.419	0.016*
AR_2	771	−2.525	0.012*
V_{CH}	895	−1.593	0.111
A_{CH}	890	−1.631	0.103
EI	930	−1.330	0.184
NSI	918	−1.420	0.156
UI	1061	−0.346	0.730
$\Delta_{\alpha\beta}$	869	−1.788	0.074
γ	734	−2.803	0.005**

**Strongly significant correlation, double-sided, $p < 0.01$; *significant correlation, double-sided, with $p < 0.05$

Table 2 Mean values ($\bar{x}$) and standard deviation (s) of the parameters D_{max}, H_{max}, AR_1, AR_2 and γ extracted with the semiautomatic neck curve approach

	D_{max} (mm)	H_{max} (mm)	AR_1	AR_2	γ (°)
Ruptured aneurysms					
$\bar{x}$	7.22	5.81	1.35	1.55	31.91
s	3.04	2.68	0.56	0.66	14.03
Unruptured aneurysms					
$\bar{x}$	6.13	4.64	1.08	1.22	44.25
s	2.74	2.37	0.47	0.53	19.14

(sidewall and bifurcation aneurysms). The presented method could extract P_1 and P_2 characterizing the transition from parent vessel to aneurysm between centerline and dome as well as P_3 and P_4 describing the bending of the NC. As illustrated in Fig. 10, the parameters extracted from the semiautomatic approach correlate well with those from the manually drawn curves. Largest differences are present for AR_1 which depends on N_{max}. This might be caused due to different bendings of the neck curves at the parent vessel.

A 3D NC determination and subsequent parameter extraction is superior to 2D measurements [4, 22], where inadequate viewing directions for the 2D projections could hamper the result, see the example in Fig. 11a. The 2D projections in clinical practice have to account for possible occlusions of surrounding vessels, and often a clear view on the parent vessel for subsequent endovascular treatment is required.

Extraction of ostium neck curves is challenging due to the wide variety of shape and size. Karmonik et al. [23] presented a 2D NC extraction which requires an analysis of vessel radius change opposite the aneurysm and could not produce the desired results for bifurcation aneurysms (see Fig. 11b). The estimation of Jerman et al. [24] is similar to our approach since ray tracing is also enabled to get the NC points. The approach by Cárdenes et al. [25] uses Voronoi diagrams for the NC extraction. Hence, a centerline inside the aneurysm is necessary.

Comparisons of the semiautomatic and manual NCs reveal a median error of 1.53 mm for the average displacements based on the metric introduced in [21]. Thus, our median average distance is definitely lower than the values reported in an additional study by Cárdenes et al. [21] comparing different neck curve extractions. They reported average median distances lower than 0.5 mm for automatic neck curve extraction methods based on deformable model extensions or geodesic curves with topological restrictions. For manual cutting plane placement, the average median distances are even lower than 0.37 mm. In consequence, these methods will yield better results w.r.t. average distance of neck curves than our approach. On the contrary, we strongly reject planar neck curves (see the example in Fig. 11d) and their dataset only comprised 26 cases.

Our approach was inspired by Neugebauer et al. [19], but we experienced several drawbacks of their method. First, the vessel radii of the parent vessel are often not identical (recall example in Fig. 11c), which caused problems for extraction of P_1 and P_2. This step also suffers from thin and bulged aneurysm shapes, where a minimum distance between the centerline and a projected centerline has to be determined. We solved this problem by restricting the possible occurrences of P_1 and P_2 to the aneurysm neck region, recall Fig. 3d. In addition, the extraction of P_3 and P_4 might stuck at local minima, i.e., bulges of the aneurysm next to the centerline can be missed, see Fig. 11c. With our method, the extraction and adaption of P_3 and P_4 prevents this problem, see the result in Fig. 12. Nevertheless, their approach was tested on seven cases, while our method could only be developed based on the large variations in the 100 datasets. On the other hand, our approach requires a pronounced neck. Although a manual selection of P_3 and P_4 can be carried out to cope with very small aneurysms without a visible neck, this is a shortcoming of our approach. An approximation of the aneurysm neck with a 2D cutting plane (as suggested in [5, 6, 9]) introduces errors when evaluating morphological parameters, since the perfect position of this plane remains unclear in case of bulging aneurysms, recall Fig. 11d.

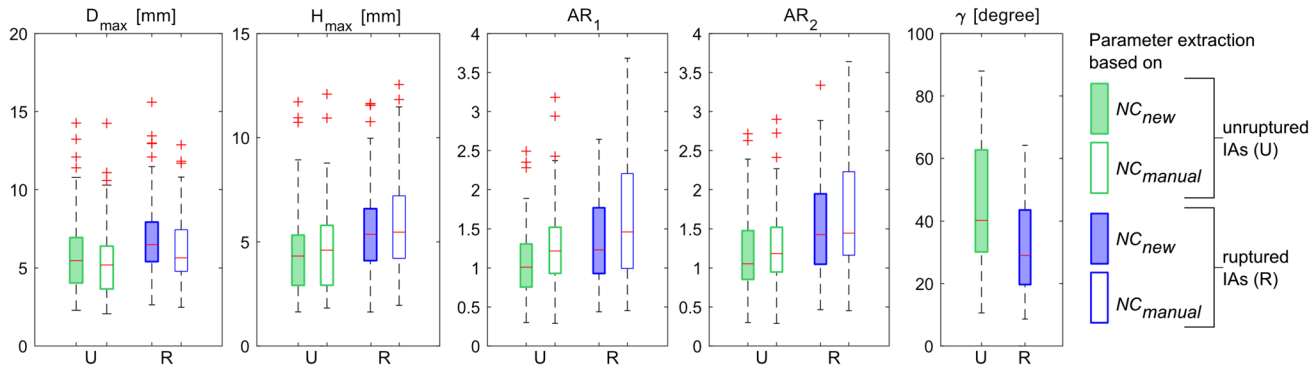

Fig. 10 Box plots of the parameters $D_{\max}$, $H_{\max}$, AR_1, AR_2 and γ extracted based on the semiautomatic neck curve approach $\mathrm{NC}_{\mathrm{new}}$ and the manually drawn neck curves $\mathrm{NC}_{\mathrm{manual}}$. Hence, γ is only available for $\mathrm{NC}_{\mathrm{new}}$. For each set of aneurysms (unruptured and ruptured), an individual box plot is provided

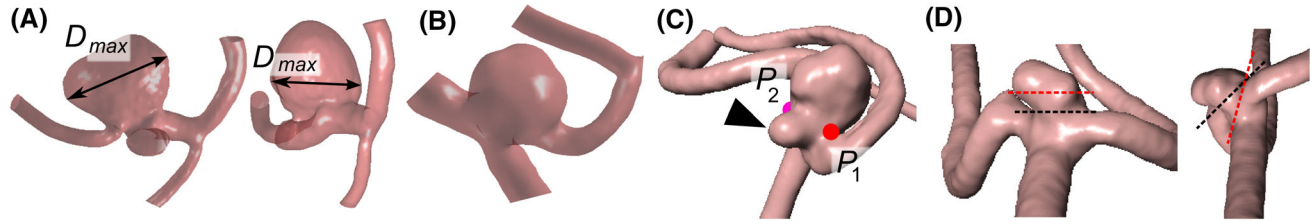

Fig. 11 Drawbacks of various approaches and specific aneurysm cases. When extracting $D_{\max}$ in 2D, the view direction influences the result (**a**). Example of a bifurcation aneurysm (**b**). Example of an aneurysm with bulges (**c**). A shortest path starting from P_1 may miss aneurysm bulges marked with an arrowhead. The plane-based approximation of the ostium is error-prone for inclined aneurysms (**d**). It is not clear if the red or the black dashed cutting plane yields the better ostium plane

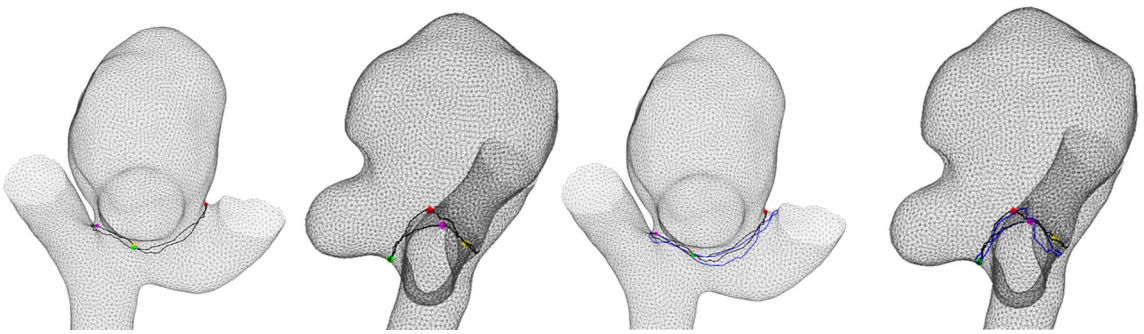

Fig. 12 Result of our NC reconstruction algorithm for the case presented in Fig. 11c (left) including the manually drawn curve (right)

The statistical evaluation of morphological parameters reveals that $D_{\max}$, $H_{\max}$, AR_1, AR_2 and γ statistically significantly correlate with the aneurysm rupture status. This is especially remarkable, since we introduce γ as characteristic angle at the dome D. Although Dhar et al. [5] introduced angle-based parameters (*aneurysm inclination angle* and *vessel angle*), we do not rely on these parameters since they are only defined for sidewall IAs and depend on the direction from which the geometry is viewed. Furthermore, the viewing direction and thus the parameter extraction had to be manually carried out in their approach. We extracted γ for all 100 aneurysms (including sidewall and bifurcation IAs) independent on the viewing direction.

Comparing them with values reported in the literature yields the following results. Lauric et al. [6] pointed out the variations for AR in the literature, arising from different definitions of aneurysm height (orthogonal height, maximum height and "depth" height which is only defined inside the aneurysm sac) and aneurysm neck diameter (maximum, average or minimum). We obtain similar values for AR_1: 1.35 ± 0.56 or 53 ruptured IAs and 1.08 ± 0.47 for 42 unruptured IAs compared to their values: 1.41 ± 0.55 for 60 ruptured and 1.14 ± 0.45 for 74 unruptured IAs. Similar results are obtained for AR_2; we obtain 1.55 ± 0.66 for ruptured and 1.22 ± 0.53 for unruptured IAs. Lauric et al. report 1.62 ± 0.74 and 1.27 ± 0.51, respectively. The definition of

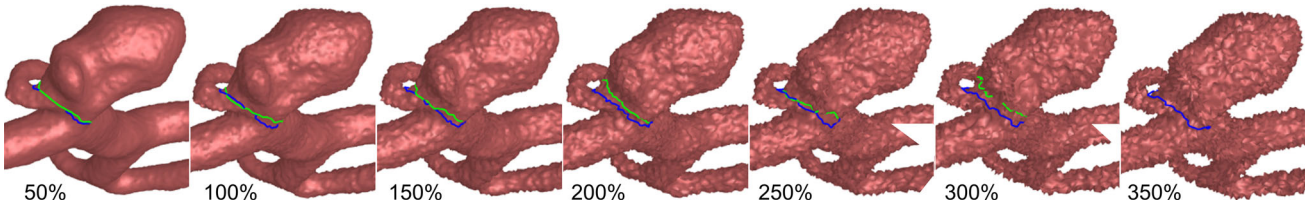

Fig. 13 Extraction of the NC (green) for triangular meshes with random noise that displaces each vertex in direction of its normal. The manual NC (blue) is provided for comparison. The percentage describes the amount of maximum displacement w.r.t. the average edge length

the aspect ratio by Dhar et al. [5] matches AR_2. They reported a mean value of 1.5 ± 0.45 for 25 ruptured and 1.2 ± 0.55 for 20 unruptured aneurysms, which agrees very well with our results.

Lauric et al. [6] report D_{max} mean values of 9.05 ± 4.00 mm and H_{max} mean values of 7.41 ± 3.55 mm for 60 ruptured and D_{max} mean values of 6.9 ± 2.78 mm and H_{max} mean values of 5.36 ± 2.37 mm for 74 unruptured IAs. These trends are reflected by our results, where ruptured IAs exhibit larger mean values than unruptured ones, but we obtain slightly different values ($D_{\text{max ruptured}} = 7.22 \pm 3.04$ mm, $D_{\text{max unruptured}} = 6.13 \pm 2.74$ mm, $H_{\text{max ruptured}} = 5.81 \pm 2.68$ mm, $H_{\text{max unruptured}} = 4.64 \pm 2.37$ mm). In addition, mean values of 6.76 ± 2.03 mm for 30 ruptured and 4.6 ± 2.85 mm for 37 unruptured IAs were reported for a slightly different D_{max} extraction in [26]. When comparing morphological measures, it must be noted that their predictive values regarding rupture risk also depend on the aneurysm location [10] and considerably variations exist regarding their definition [6]. We account for this problem by extracting different variations of the aspect ratio yielding AR_1 and AR_2 instead of a single parameter. Hence, future studies and clinical trials should provide information and standardized guidelines which method is preferable.

Due to the high correlations between the morphological parameters D_{max}, H_{max}, AR_1, AR_2 and γ, it may be not necessary to extract all of them. Future work should evaluate different classifiers based on different parameter sets w.r.t their discriminative power. Since extraction of γ does not require the complete NC but only D, B_1 and B_2 (i.e., only Step 2 of our pipeline, depicted in Fig. 1b), a future classification approach could be speed up. Initial experiments identified γ and the *EI* as most important parameters based on our training dataset for a gradient-boosted tree classifier. Hence, a combination of parameters is superior to the usage of a single one. Future work can reveal which combination of the presented parameters yields best prediction results. Dhar et al. [5] also carried out multivariate logistic regression analysis stating that only two of their five parameters were identified as independently significant; the size ratio and the undulation index *UI*. Regarding the effect size of our approach, we achieved only a small effect [27] due to the large sample size.

We do not evaluate interaction effects yet. Although all significant parameters correlate with each other maybe interaction effects between nonsignificant parameters can be examined. This will be part of a subsequent analysis. In addition, a prospective study comprising untreated longitudinal IAs is of great interest, but these datasets are rare in clinical practice.

For the assessment of artifacts due to noise, we added artificial random noise to the triangle meshes inspired by [28]. An example for case 53 is provided in Fig. 13. Therefore, each vertex of the surface mesh was randomly displaced in direction of its surface normal. The maximum amount of the displacement for each step was determined by the percentaged average edge length of the triangle mesh. With a noise level that randomly alters vertices up to 300% of the average edge length, the NC could still be successfully extracted. Only with a noise level of 350%, the identification of V_1 and V_2 was not possible anymore, see Fig. 13.

For the 100 aneurysms, no manual correction was required. The reproducibility of our method depends on the centerline, D_{Start} and parameters t and s. For centerline extraction, we employ an already well-established method [18]. D_{Start} does not influence D in a mesh where D has the largest distance to the centerline. If there is noise present, D may be found at the local maximum. A post-processing step could further reduce this variability, by first separating the aneurysm from the parent vessel and then repeat the procedure but using the separated aneurysm for possible locations of D instead the neighbored surface vertices of D_{Start}. Parameters t and s do influence the result, but we provide default values such that the same NC is extracted.

A ground truth for neck curves is not available yet. Future work could include more manual drawn neck curves from more clinical experts; however, manual definition is a very time-consuming task. Furthermore, errors during manual drawing may occur as well especially for complex and irregularly shaped aneurysms.

Beside the precise morphological evaluation of the 3D aneurysm shape, an automatized ostium detection is highly beneficial for the quantification of hemodynamic flow simulations [29]. Particularly, since relevant blood flow parameters that are associated with rupture (e.g., normalized wall shear stress, shear concentration index, oscillatory shear

index [30]) need to be calculated with high accuracy, wrong aneurysm-vessel-separation or high user-dependency can lead to clear variations regarding the analysis.

Conclusions

We presented a semiautomatic 3D NC reconstruction algorithm which yields reproducible results and was successfully applied to 100 IAs. The employed IA triangle surface meshes are based on segmented rotational angiography images. However, the approach is suitable for segmented CTA and MRA datasets as well. The NC reconstruction yields an anatomical shaped curve, i.e., the NC does not lie in a plane. It allows for automatic extraction of common morphological parameters as well as a newly introduced characteristic angle γ at the aneurysm's dome. Statistical evaluation yields statistical significant correlation of the morphological parameters $D_{\max}$, $H_{\max}$, AR_1 and AR_2 with rupture status which is in good agreement with the literature. Thus, the 3D NC reconstruction is well suited for further applications including the quantification of hemodynamic flow simulations. The newly introduced characteristic angle γ at the dome yields statistical significance as well and correlates with the other morphological parameters indicative for rupture status. Considering that γ can be extracted at a very early stage of our method relying on B_1 and B_2 but not on the complete NC, a benefit for future classifiers is expected.

Acknowledgements The work was funded by the Federal Ministry of Education and Research within the Forschungscampus *STIMULATE* under Grant No. "13GW0095A."

Compliance with ethical standards

Conflict of interest The authors declare that they have no conflict of interest.

Ethical approval All procedures performed in studies involving human participants were in accordance with the ethical standards of the institutional and/or national research committee and with the 1964 Declaration of Helsinki and its later amendments or comparable ethical standards. For this type of study, formal consent is not required.

Informed consent Informed consent was obtained from all individual participants included in the study.

References

1. Meng H, Tutino VM, Xiang J, Siddiqui A (2014) High WSS or low WSS? complex interactions of hemodynamics with intracranial aneurysm initiation, growth, and rupture: toward a unifying hypothesis. Am J Neuroradiol 35(7):1254–1262
2. Weir B, Amidei C, Kongable G, Findlay JM, Kassell NF, Kelly J, Dai L, Karrison TG (2003) The aspect ratio (dome/neck) of ruptured and unruptured aneurysms. J Neurosurg 99(3):447–451
3. Backes D, Vergouwen MD, Velthuis BK, van der Schaaf IC, Bor ASE, Algra A, Rinkel GJ (2014) Difference in aneurysm characteristics between ruptured and unruptured aneurysms in patients with multiple intracranial aneurysms. Stroke 45(5):1299–1303
4. Wong SC, Nawawi O, Ramli N, Kadir KAA (2012) Benefits of 3D rotational DSA compared with 2D DSA in the evaluation of intracranial aneurysm. Acad Radiol 19(6):701–707
5. Dhar S, Tremmel M, Mocco J, Kim M, Yamamoto J, Siddiqui AH, Hopkins LN, Meng H (2008) Morphology parameters for intracranial aneurysm rupture risk assessment. Neurosurgery 63(2):185–196 **(discussion 196–7)**
6. Lauric A, Baharoglu MI, Malek AM (2012) Ruptured status discrimination performance of aspect ratio, height/width, and bottleneck factor is highly dependent on aneurysm sizing methodology. Neurosurgery 71(1):38–45
7. Lv N, Wang C, Karmonik C, Fang Y, Xu J, Yu Y, Cao W, Liu J, Huang Q (2016) Morphological and hemodynamic discriminators for rupture status in posterior communicating artery aneurysms. PLoS ONE 11(2):e0149906
8. Miura Y, Ishida F, Umeda Y, Tanemura H, Suzuki H, Matsushima S, Shimosaka S, Taki W (2013) Low wall shear stress is independently associated with the rupture status of middle cerebral artery aneurysms. Stroke 44(2):519–521
9. Raghavan ML, Ma B, Harbaugh RE (2005) Quantified aneurysm shape and rupture risk. J Neurosurg 102(2):355–362
10. Varble N, Rajabzadeh-Oghaz H, Wang J, Siddiqui A, Meng H, Mowla A (2017) Differences in morphologic and hemodynamic characteristics for "PHASES-based" intracranial aneurysm locations. Am J Neuroradiol 38(11):2105–2110
11. Xiang J, Natarajan SK, Tremmel M, Ma D, Mocco J, Hopkins LN, Siddiqui AH, Levy EI, Meng H (2011) Hemodynamic-morphologic discriminants for intracranial aneurysm rupture. Stroke 42(1):144–152
12. Berg P, Saalfeld S, Voß S, Redel T, Preim B, Janiga G, Beuing O (2017) Does the DSA reconstruction kernel affect hemodynamic predictions in intracranial aneurysms? an analysis of geometry and blood flow variations. J Neurointerventional Surg. https://doi.org/10.1136/neurintsurg-2017-012996
13. Neugebauer M, Lawonn K, Beuing O, Berg P, Janiga G, Preim B (2013) AmniVis—a system for qualitative exploration of near-wall hemodynamics in cerebral aneurysms. Comput Graph Forum 32(3):251–260
14. Janiga G, Berg P, Beuing O, Neugebauer M, Gasteiger R, Preim B, Rose G, Skalej M, Thévenin D (2013) Recommendations for accurate numerical blood flow simulations of stented intracranial aneurysms. Biomed Eng 58(3):303–314
15. Saalfeld P, Luz M, Berg P, Preim B, Saalfeld S (2017) Guidelines for quantitative evaluation of medical visualizations on the example of 3D aneurysm surface comparisons. Comput Graph Forum 27(5):347
16. Glaßer S, Berg P, Voß S, Serowy S, Janiga G, Preim B, Beuing O (2016) From imaging to hemodynamics—how reconstruction kernels influence the blood flow predictions in intracranial aneurysms. Curr Dir Biomed Eng 2(1):163
17. Glaßer S, Berg P, Neugebauer M, Preim B (2015) Reconstruction of 3D surface meshes for blood flow simulations of intracranial aneurysms. In: Proceeding of the computer- and robot-assisted surgery (CURAC), pp 163–168
18. Antiga L, Piccinelli M, Botti L, Ene-Iordache B, Remuzzi A, Steinman DA (2008) An image-based modeling framework for patient-specific computational hemodynamics. Med Biol Eng Compu 46(11):1097–1112

19. Neugebauer M, Diehl V, Skalej M, Preim B (2010) Geometric reconstruction of the ostium of cerebral aneurysms. In: Proceeding of the vision modeling visualization (VMV), pp 307–314
20. Dijkstra EW (1959) A note on two problems in connexion with graphs. Numer Math 1(1):269–271
21. Cárdenes R, Larrabide I, San Román L, Frangi AF (2013) Performance assessment of isolation methods for geometrical cerebral aneurysm analysis. Med Biol Eng Compu 51(3):343–352
22. Ma B, Harbaugh RE, Raghavan ML (2004) Three-dimensional geometrical characterization of cerebral aneurysms. Ann Biomed Eng 32(2):264–273
23. Karmonik C, Arat A, Benndorf G, Akpek S, Klucznik R, Mawad ME, Strother CM (2004) A technique for improved quantitative characterization of intracranial aneurysms. Am J Neuroradiol 25(7):1158–1161
24. Jerman T, Pernuš F, Likar B, Špiclin Ž (2015) Computer-aided detection and quantification of intracranial aneurysms. In: Proceeding of the medical image computing and computer-assisted intervention (MICCAI). Lecture notes in computer science, vol 9350, pp 3–10
25. Cárdenes R, Pozo JM, Bogunovic H, Larrabide I, Frangi AF (2011) Automatic aneurysm neck detection using surface Voronoi diagrams. IEEE Trans Med Imaging 30(10):1863–1876
26. Hoh BL, Sistrom CL, Firment CS, Fautheree GL, Velat GJ, Whiting JH, Reavey-Cantwell JF, Lewis SB (2007) Bottleneck factor and height-width ratio: association with ruptured aneurysms in patients with multiple cerebral aneurysms. Neurosurgery 61(4):716–723
27. Cohen J (1988) Statistical power analysis for the behavioral sciences. Erlbaum, New York
28. Neugebauer M, Lawonn K, Beuing O, Preim B (2013) Automatic generation of anatomic characteristics from cerebral aneurysm surface models. Int J Comput Assist Radiol Surg (JCARS) 8(2):279–289
29. Berg P, Beuing O (2018) Multiple intracranial aneurysms: a direct hemodynamic comparison between ruptured and unruptured vessel malformations. Int J Comput Assist Radiol Surg (JCARS) 13(1):83–93
30. Cebral JR, Mut F, Weir J, Putman C (2011) Quantitative characterization of the hemodynamic environment in ruptured and unruptured brain aneurysms. Am J Neuroradiol (AJNR) 32(1):145–151